RSC Applied Interfaces

ROYAL SOCIETY OF CHEMISTRY

PAPER

View Article Online
View Journal | View Issue

Cite this: *RSC Appl. Interfaces*, 2025, **2**, 684

High-efficiency CuO-CB6/Co–Al LDH nanocomposite electrode for next-generation energy storage†

Anakha D. R.,[ab] Ashika K. M.,‡[ab] Vyshnavi T. V.,‡[ab] M. Ananthkumar[c] and R. Yamuna*[ab]

Supercapacitors are a highly effective choice for energy storage applications. The high specific power, quick charge–discharge time, and inexpensive upkeep of supercapacitors have sparked immense interest in the energy industry and research. The advancement of high-quality supercapacitors depends heavily on the exploitation of composite electrode materials. This study involves the synthesis of cucurbit[6]uril-stabilized CuO nanoparticles (CuO-CB6 NPs) using a simple reduction method, which were then integrated onto cobalt–aluminium layered double hydroxide (Co–Al LDH) in three different ratios (1 : 1, 1 : 2, and 2 : 1) to create CuO-CB6/Co–Al LDH nanocomposites. The structural and chemical properties of the suggested nanocomposites are analyzed using various spectroscopic techniques. The electrochemical performance of CuO-CB6, Co–Al LDH, and CuO-CB6/Co–Al LDH nanocomposites is evaluated using CV, GCD, and EIS measurements. The electrochemical performance of the 1 : 2 CuO-CB6/Co–Al LDH nanocomposite reveals a notable specific capacitance of 1862 F g^{-1} at a current density of 0.45 A g^{-1}. Electrochemical impedance analysis indicates a low charge transfer resistance value and thereby enhanced electrical conductivity for the nanocomposite. The 1 : 2 CuO-CB6/Co–Al LDH nanocomposite demonstrates significant long-term cycling stability, retaining 79% of its initial specific capacitance after 10 000 cycles at a current density of 7.27 A g^{-1}. These findings suggest that the 1 : 2 CuO-CB6/Co–Al LDH nanocomposite exhibits improved electrochemical performance and can be used as an electrode material for supercapacitor applications.

Received 18th December 2024,
Accepted 17th January 2025

DOI: 10.1039/d4lf00417e

rsc.li/RSCApplInter

Introduction

In recent decades, there has been a substantial rise in energy demand which is attributed to the rapid depletion of fossil fuels, the increasing need for electronic devices, and the rising production of electric and hybrid vehicles. Consequently, the advancement of clean, sustainable, and efficient energy storage technologies is crucial for the global scientific and technological communities. This has prompted the necessity for rapid advancements in electrochemical energy storage technologies, encompassing fuel cells, supercapacitors, batteries, and various other devices.[1–4] Among the devices addressed, supercapacitors exhibit enhanced energy-delivery capabilities and can store a comparatively higher energy density than conventional capacitors. Supercapacitors are extensively utilized in various applications, such as electronics, smart grids, aircraft, and hybrid or electric vehicles owing to their numerous advantages, which encompass rapid charging, extended charge–discharge cycles, and a broad operational temperature range.[5–7] Supercapacitors can be classified into three primary categories: electric double-layer capacitors (EDLCs), pseudocapacitors, and hybrid supercapacitors. In EDLCs, energy is stored in strong electric fields through the double-layer capacitance mechanism, also referred to as non-faradaic. On the other hand, pseudocapacitors store electricity through fast, reversible faradaic redox reactions that happen on the electrode surface.[8–10] EDLCs utilize carbon aerogels, graphene, carbon nanotubes, and activated carbon as electrode materials, while pseudocapacitors incorporate conducting polymers and metal oxides.[11] Recently, the advancement of hybrid supercapacitors that exhibit both pseudo-capacitance and EDL capacitance has garnered

[a] *Department of Chemistry, Amrita School of Physical Sciences Coimbatore, Amrita Vishwa Vidyapeetham, India. E-mail: r_yamuna@cb.amrita.edu*
[b] *Bio-materials Chemistry Research Laboratory, Amrita School of Engineering Coimbatore, Amrita Vishwa Vidyapeetham, India*
[c] *Department of Civil Engineering, Amrita School of Engineering Coimbatore, Amrita Vishwa Vidyapeetham, India*

† Electronic supplementary information (ESI) available: Electrochemical calculation procedure, FT-IR, XRD, CV, GCD, and EIS for 1 : 1 & 2 : 1 nanocomposites, EDX of Co–Al LDH and XPS C & O 1s of 1 : 2. See DOI: https://doi.org/10.1039/d4lf00417e

‡ Equal contribution.

significant attention.[12,13] The materials used for electrodes significantly impact the capacitance and charge storage capabilities of a supercapacitor.

Recently, there has been enormous interest in studies on layered double hydroxides (LDHs), a form of anionic clay made up of positively charged metal hydroxide layers interspersed with charge-balancing anions and water molecules.[14,15] LDHs present a convincing option for electrode materials, attributed to their cost-effective synthesis, robust electrochemical performance, elevated specific capacitance (SC), and adjustable composition.[16] However, the limitation of LDHs lies in their relatively low mass diffusion and electron transfer rates, which restrict their capacity for high rate charging and discharging, thereby reducing their efficacy as electrode materials. Recently, researchers have developed a growing number of advanced and innovative nanoarchitectures based on LDHs to improve the pseudocapacitive performance. These nanoarchitectures include hollow LDH spheres, conducting polymer/LDH core–shell nanosheet arrays, and metal oxides/LDHs.

A significant amount of investigation has shown the importance of transition metal oxides as intriguing materials for supercapacitor electrodes due to their beneficial structural, mechanical, and electrical characteristics, along with their substantial pseudocapacitance, economical production, and excellent environmental stability.[17,18] Numerous significant transition metal oxides, including MnO_2, NiO, CuO, Co_3O_4, and Fe_3O_4, have undergone thorough investigation. Among these, CuO nanoparticles (NPs) acquired significant attention as a promising electrode material.[17]

The abundance of copper metal has motivated us to execute the synthesis and subsequently perform the electrochemical testing of cucurbit[6]uril (CB6)-stabilized CuO NPs (CuO-CB6) for an electrode material. CB6 is a non-polar macrocyclic compound that is easily produced by condensation of formaldehyde and glycoluril. The hydrophobic cavities of CB6 feature portals lined with C═O groups which enhance the binding of cations *via* hydrogen bonding or ion–dipole interactions. CB6 demonstrates significant potential as a component of molecular machines due to its superior binding selectivity and precise chemical control over size and shape.[19] Copper oxide is a common metal oxide that is readily available and exhibits high SC in faradaic and non-faradaic electrode materials. Several studies have been conducted on the electrochemical energy storage of different types of copper oxide NPs and their nanocomposites. Kunhikrishnan *et al.* synthesized a sphere-like CuO nanostructure utilizing cetyl trimethyl ammonium bromide, demonstrating a SC of 468 F g^{-1} at a current density (CD) of 1 A g^{-1}.[20] Zhan *et al.* presented biomass-derived porous carbon integrated with CuO NPs, demonstrating a SC of 530 F g^{-1} at a CD of 1 A g^{-1}.[21] Eivazzadeh-Keihan *et al.* developed a rGO/CuO/PpPD nanocomposite that exhibited a remarkable SC of 512.12 F g^{-1} at a CD of 1 A g^{-1}.[22] Ahmad *et al.* presented the CuO@PANiNFs electrode, achieving a remarkable SC of 486.9 F g^{-1} at a CD of 0.5 mA cm^{-2}.[23] Further, supercapacitor studies involving CoAl-LDH have also been reported in the literature. Peng *et al.* developed fluorinated graphene/CoAl-LDH composites that exhibit remarkable rate performance, excellent recyclability, and a high SC of 1222 F g^{-1} at a CD of 1 A g^{-1}.[24] Hierarchical CoAl-LDH/MnO_2 composites produced by Diao *et al.* exhibited a remarkable SC of 1088 F g^{-1} at a CD of 1 A g^{-1}.[25]

The aim of this study is to develop efficient nanocomposites of the type CuO-CB6/Co–Al LDH by integrating CuO-CB6 onto cobalt–aluminium layered double hydroxide (Co–Al LDH) in three different ratios (1 : 1, 1 : 2, and 2 : 1). Further, these nanocomposites are effectively fabricated as electrode materials for supercapacitor applications. The formation of CuO-CB6, Co–Al LDH, and CuO-CB6/Co–Al LDH (1 : 1, 1 : 2, and 2 : 1) nanocomposites has been validated through different characterization techniques. The electrochemical performance of the pristine materials and all the nanocomposites is analyzed through cyclic voltammetry (CV), galvanostatic charge–discharge (GCD), and electrochemical impedance spectroscopic (EIS) techniques.

Experimental section

Materials and instrumentation

Glycoluril, formaldehyde, and $Cu(NO_3)_2{\cdot}3H_2O$ were procured from TCI, Merck, and NICE Chemicals, respectively. Carbon black, potassium hydroxide (KOH), polyvinylidene fluoride (PVDF), *N*-methyl-2-pyrrolidone (NMP), and sodium borohydride ($NaBH_4$) were obtained from Sigma-Aldrich. NH_4F and $Co(NO_3)_2{\cdot}6H_2O$ were bought from Avra. Urea and $Al(NO_3)_3{\cdot}9H_2O$ were purchased from Fisher Scientific Chemicals and Rankem, respectively.

Fourier transform infrared (FT-IR) spectra of CuO-CB6, Co–Al LDH, and CuO-CB6/Co–Al LDH nanocomposites were determined in ATR mode (Bruker-ALPHA-Platinum spectrophotometer) with a spectral range of 4000 to 400 cm^{-1}. The crystallinity of CuO-CB6, Co–Al LDH, and CuO-CB6/Co–Al LDH was obtained through X-ray diffraction (Malvern Panalytical multipurpose XRD) using Cu Kα radiation in the diffraction angle (2θ) range of 10–70° with a step size of 0.02°, at 40 kV and 30 mA. Field emission scanning electron microscopy (FE-SEM) (Carl Zeiss, Zeiss Gemini SEM 300) with energy dispersive X-ray spectroscopy (EDX) analysis was employed to characterize the morphology and composition of Co–Al LDH and 1 : 2 CuO-CB6/Co–Al LDH. HR-TEM images of CuO-CB6 and 1 : 2 CuO-CB6/Co–Al LDH were recorded using a TEM operating at an accelerating voltage of 200 kV (Jeol/JEM 2100). Specific surface areas and pore size distribution of 1 : 2 CuO-CB6/Co–Al LDH were determined by using the Autosorb iQ Station 1 volumetric adsorption analyzer through Brunauer–Emmett–Teller (BET) analysis. X-ray photoelectron spectroscopy (XPS) analysis of 1 : 2 CuO-CB6/Co–Al LDH was performed using a KRATOS Axis Ultra instrument equipped with Al Kα = 1486.6 eV. The supercapacitor performance of CuO-CB6, Co–Al LDH, 1 : 2

CuO-CB6/Co–Al LDH, 2 : 1 CuO-CB6/Co–Al LDH, and 1 : 1 CuO-CB6/Co–Al LDH was measured on an electrochemical workstation (BioLogic SP-240).

Synthesis of CuO-CB6

Precursor CB6 was synthesized by an acid-catalyzed condensation reaction of glycoluril and formaldehyde, as reported previously.[26] CuO-CB6 was synthesized by a simple reduction method.[27] Generally, CB6 (0.050 g, 0.050 mmol) was dissolved in a 0.100 N aqueous K_2CO_3 solution, and $Cu(NO_3)_2{\cdot}3H_2O$ (0.040 g, 0.165 mmol) was then added in a round-bottom flask. The mixture was briefly sonicated and then stirred for one hour in an argon atmosphere using a magnetic stirrer. Subsequently, a freshly prepared $NaBH_4$ reducing agent (0.825 mmol in 2 mL water) was added dropwise in a 1 : 5 molar ratio to the metal precursor while stirring in an argon atmosphere for 2 h. Finally, a black precipitate indicating the production of CuO-CB6 was obtained by centrifugation at 1500 rpm for 15 min and dried at 80 °C in a vacuum.

Preparation of CuO-CB6/Co–Al LDH nanocomposites

Precursor Co–Al LDH was synthesized using the urea hydrolysis method, as reported elsewhere.[28] We developed three different nanocomposites of CuO-CB6/Co–Al LDH using the wet impregnation method, combining 1 : 1, 1 : 2, and 2 : 1 compositions of Co–Al LDH and CuO-CB6. They were designated as 1 : 1 CuO-CB6/Co–Al LDH, 1 : 2 CuO-CB6/Co–Al LDH, and 2 : 1 CuO-CB6/Co–Al LDH, respectively. Typically, CuO-CB6 and Co–Al LDH were taken in a 1 : 2 ratio in 8 mL of DMSO solvent and ultrasonicated for 0.5 h. This was then subjected to heating at 50 °C for 3 h and stirred for 24 h to obtain the CuO-CB6/Co–Al LDH nanocomposite. The synthesized nanocomposite was centrifuged and dried under vacuum at 100 °C. For comparison, other composites of 1 : 1 CuO-CB6/Co–Al LDH and 2 : 1 CuO-CB6/Co–Al LDH were also prepared using the same procedure. Fig. 1 depicts the synthetic pathway of the CuO-CB6/Co–Al LDH nanocomposite from the pristine CuO-CB6 and Co–Al LDH.

Electrochemical measurements of CuO-CB6, Co–Al LDH, and CuO-CB6/Co–Al LDH nanocomposites

The electrochemical measurements of all the synthesized CuO-CB6, Co–Al LDH, and CuO-CB6/Co–Al LDH nanocomposites were carried out in a three-electrode cell setup on an electrochemical (BioLogic SP-240) workstation at room temperature using 1 M KOH as the electrolyte. The electrocatalytic slurry was prepared using the synthesized material, carbon black, and PVDF in a weight ratio of 8 : 1 : 1 along with 3 μL of NMP solvent. The freshly prepared slurry was subsequently applied onto a Ni foam that had been pre-cleaned, with an area of 1 cm × 1 cm. After drying, the coated nickel foam was used directly as the working electrode. The active electrode material utilized in the experiment had a mass of approximately 2.2 mg. A graphite electrode and Hg/HgO were employed as the counter and reference electrode, respectively. The fabricated nickel foam was used as the working electrode, which was modified with synthesized CuO-CB6, Co–Al LDH, and CuO-CB6/Co–Al LDH nanocomposites. Electrochemical methods, including CV, GCD, and EIS, were employed to investigate the synthesized catalyst's electrochemical performance, stability and charge transfer resistance. The specific capacitance, energy density, and power density of the three-electrode setup were determined as reported in the literature, and the calculation procedures are presented in the ESI† section S1.

Results and discussion

Physicochemical characterization of CuO-CB6/Co–Al LDH nanocomposites

The interaction between Co–Al LDH and CB6-capped CuO NPs likely encompasses electrostatic and hydrogen bonding interactions. The positively charged metal hydroxide layers of Co–Al LDH may electrostatically interact with the partial negatively charged surface of CuO NPs and particularly the carbonyl portal on the CB6 capping agent. Moreover, hydrogen bonding may take place between the hydroxyl groups on the LDH layers and possible hydrogen bond acceptors on the CB6 or CuO surface. These forces of interaction may be responsible for the dispersion of CB6-stabilized CuO NPs within the Co–Al LDH matrix, thereby further influencing the composite's effectiveness in energy storage applications.

FT-IR spectral studies were executed to analyse the structural characteristics of synthesized CuO-CB6, Co–Al LDH, and 1 : 2 CuO-CB6/Co–Al LDH as illustrated in Fig. 2a. CuO-CB6's spectrum depicts prominent vibrational peaks due to the presence of CB6 capping agent at 1727, 1481,

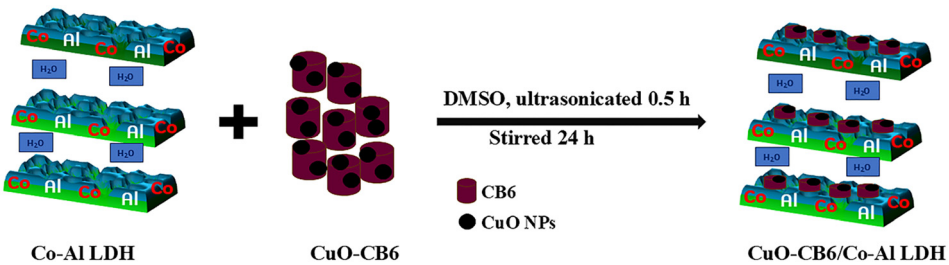

Fig. 1 Synthetic pathway of the CuO-CB6/Co–Al LDH nanocomposite.

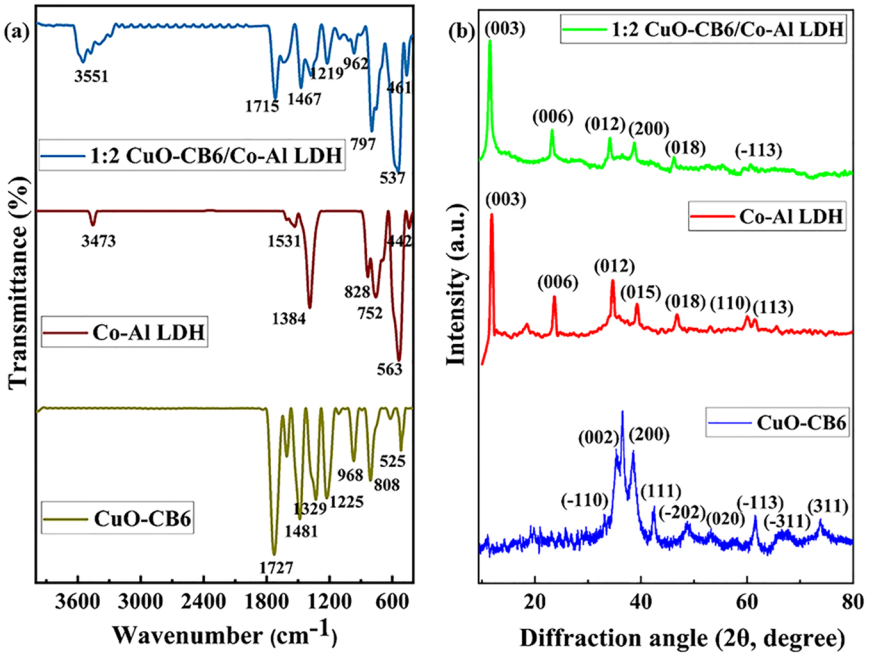

Fig. 2 (a) FT-IR and (b) XRD spectra of CuO-CB6, Co–Al LDH, and 1 : 2 CuO-CB6/Co–Al LDH.

1329, and 1225 cm^{-1}, which can be ascribed to the stretching vibrations of C═O, C–O, C–N, and C–C, respectively. Further, it reveals a methylene C–H bending vibrational peak at 968 cm^{-1} and a CH_2 rocking vibrational peak at 808 cm^{-1}.[29] The presence of a metal–oxygen [Cu(II)–O] stretching vibrational peak at 525 cm^{-1} apart from other characteristic peaks of CB6 supports the formation of CB6 stabilized CuO NPs.[27,30] The characteristic band of Co–Al LDH detected around 3473 cm^{-1} is related to the hydrogen-bonded OH groups and O–H stretching vibration of interlayer water molecules. The bending mode of interlayer water molecules may be the primary cause of the signal at 1531 cm^{-1}. The peaks observed at 1384, 828, and 752 cm^{-1} indicate the intercalation of carbonate ions into LDHs and correspond to the bending vibration mode of CO_3^{2-}. The band at 442 cm^{-1} is attributed to the M–O stretching mode, whereas the band at 563 cm^{-1} corresponds to the M–OH bending vibration mode of Co–Al LDH.[31] The FT-IR spectrum of 1 : 2 CuO-CB6/Co–Al LDH displays multiple vibration bands, including stretching mode of Cu(II)–O, C═O, C–O, C–N, C–C, C–H, O–H and bending vibrations of the methylene group. Nonetheless, the positions of these bands are shifted in comparison to the pristine CuO-CB6 and Co–Al LDH, suggesting the formation of the 1 : 2 CuO-CB6/Co–Al LDH nanocomposite. FT-IR spectra of CuO-CB6/Co–Al LDH (1 : 1 and 2 : 1) are depicted in the ESI,† Fig. S1. Therefore, the FT-IR analysis emphasises the formation of CuO-CB6/Co–Al LDH, CuO-CB6, and Co–Al LDH.

Fig. 2b illustrates the XRD pattern of CuO-CB6, Co–Al LDH, and 1 : 2 CuO-CB6/Co–Al LDH nanocomposite. The XRD patterns of 1 : 1 CuO-CB6/Co–Al LDH and 2 : 1 CuO-CB6/Co–Al LDH are illustrated in the ESI† Fig. S2. The crystal phase of CuO NPs is compatible with JCPDS and ICDD card nos. 45-0937 and 801916, respectively[32,33] for the diffraction pattern, as illustrated in Fig. 2b. The standard peaks at 32.46, 35.48, 38.62, 42.35, 48.73, 53.52, 57.83, 61.44, 65.75, 67.87, 73.61, and 74.92° correspond to the miller indices (−110), (002), (200), (111), (−202), (020), (202), (−113), (−311), (113), (311), and (−222), respectively. These peaks reveal the space group symmetry of *C*2/*c* with monoclinic structure of copper. The average crystallite size of CuO NPs was determined using the Debye–Scherrer formula and the calculated value is 14 nm. The diffractograms of Co–Al LDH (Fig. 2b) exhibit distinct peaks at 2θ = 11.8, 23.6, 34.7, 39.1, 46.8, 60.0, and 61.4°, corresponding to the (003), (006), (012), (015), (018), (110), and (113) crystal planes, respectively, which are in close agreement with the JCPDS and ICDD card nos. 51-0045 and 01-076-3252, respectively for Co–Al LDH.[31,34] The XRD peak indicated a hexagonal cell exhibiting rhombohedral symmetry ($R\bar{3}m$). This confirms the successful preparation of Co–Al LDH. In Fig. 2b, the XRD pattern of 1 : 2 CuO-CB6/Co–Al LDH reveals diffraction peaks at 38.58 and 61.14° that are associated with CuO NPs. These peaks are shifted to lower angles as compared to pristine CuO-CB6 NPs. Similarly, when comparing the XRD patterns of pure Co–Al LDH and 1 : 2 CuO-CB6/Co–Al LDH, the peaks corresponding to the (003), (006), (012), and (018) planes are also shifted to lower angles. The confinement of CuO-CB6 within Co–Al LDH accounts for the shift towards lower angles. Additionally, ESI† Fig. S2 displays the XRD patterns of 1 : 1 CuO-CB6/Co–Al LDH and 2 : 1 CuO-CB6/Co–Al LDH. 1 : 1 CuO-CB6/Co–Al LDH and 2 : 1 CuO-CB6/Co–Al LDH exhibit comparable shifts to lower angles in the (002) and (200) planes of CuO-CB6, as well as the (006), (012), (018), and (110) planes of Co–Al LDH.

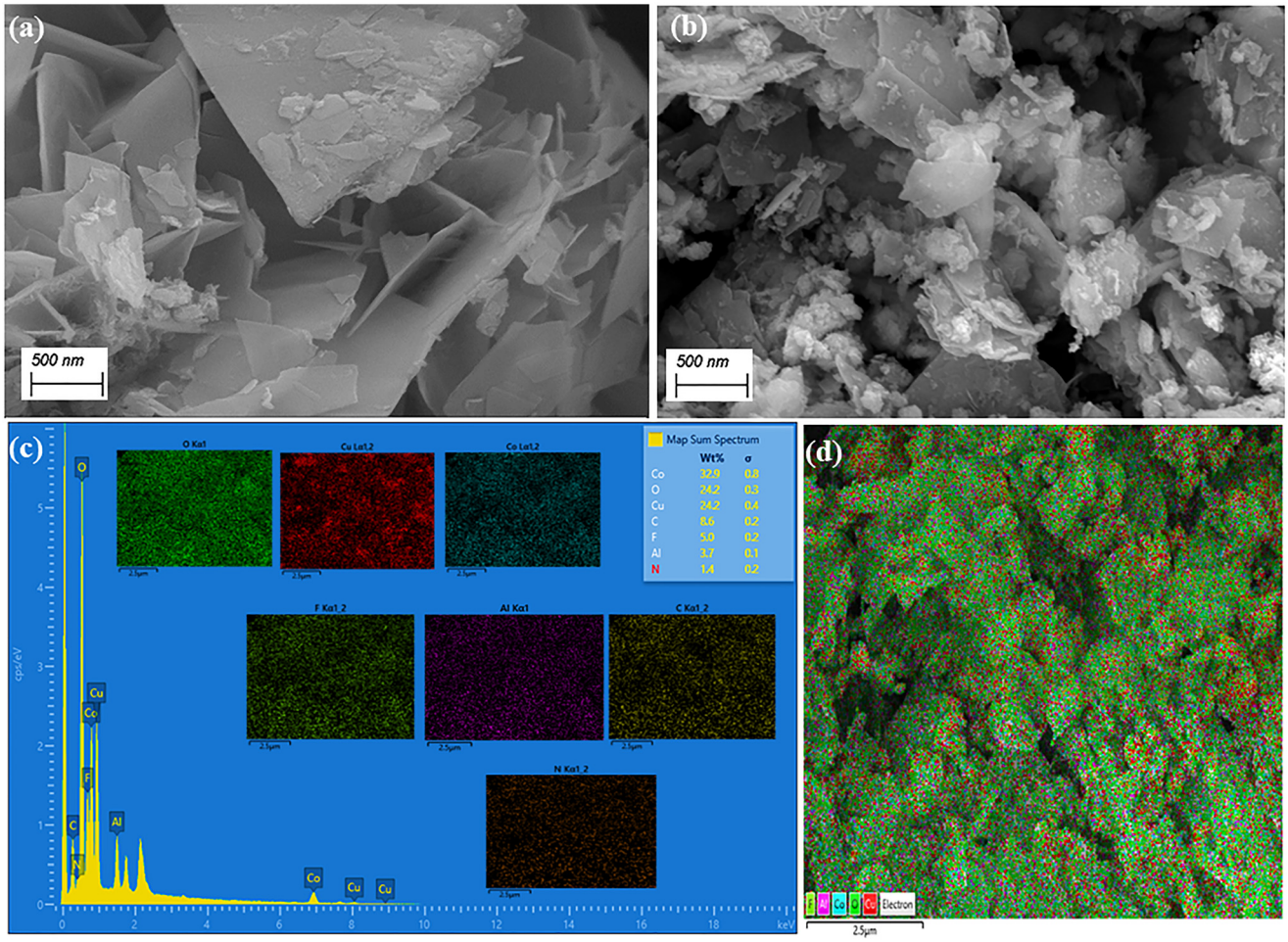

Fig. 3 FE-SEM images of (a) Co–Al LDH and (b) 1 : 2 CuO-CB6/Co–Al LDH, (c) EDX spectrum and (d) EDS layered images of 1 : 2 CuO-CB6/Co–Al LDH.

The surface analysis and elemental data of Co–Al LDH and 1 : 2 CuO-CB6/Co–Al LDH are examined using FE-SEM and EDX techniques, as illustrated in Fig. 3 and ESI† Fig. S3. The FE-SEM image of Co–Al LDH exhibited the characteristic smooth nanosheet morphology, aligning with previous reports on LDH materials.[35,36] The presence of spherical shaped CuO-CB6 nanoparticles in between the layers of Co–Al LDH as shown in Fig. 3b confirms the formation of 1 : 2 CuO-CB6/Co–Al LDH. The EDX spectrum and elemental mapping analysis of Co–Al LDH confirm the presence of elements like Co, Al, C, and O as shown in the ESI† Fig. S3. Further Fig. 3c and d clearly exemplify the uniform arrangement of elements like Cu, Co, Al, O, N, and C in the nanocomposite. Therefore, this SEM surface analysis clearly proves the existence of CuO-CB6 in between the layers of Co–Al LDH in the nanocomposite.

HR-TEM and SAED are competent tools for acquiring accurate structural data on nanocomposites. Fig. 4a–e illustrate the TEM and SAED patterns for CuO-CB6 and 1 : 2 CuO-CB6/Co–Al LDH. The HR-TEM image of CuO-CB6 (Fig. 4a) demonstrates a uniform distribution of spherical CuO NPs on the surface of the CB6 matrix.[27] The HR-TEM images of the as-synthesized 1 : 2 CuO-CB6/Co–Al LDH morphologies indicate the presence of spherical CuO-CB6 NPs in between the Co–Al LDH layers as shown in Fig. 4b and c. Fig. 4d and e illustrate the SAED patterns of CuO-CB6 and 1 : 2 CuO-CB6/Co–Al LDH, respectively, displaying scattered spots accompanied by several rings. These observations, along with the lack of consistent bright spots, confirm the polycrystalline characteristics of CuO-CB6 and 1 : 2 CuO-CB6/Co–Al LDH. Thus, HR-TEM analysis confirms the fabrication of the 1 : 2 CuO-CB6/Co–Al LDH nanocomposite.

A large surface area and an ideal pore size distribution are known to be important for improving the performance of electrode materials used in supercapacitors.[31,37] The analyses of nitrogen adsorption/desorption isotherms were conducted at 77.35 K to investigate the specific surface area and pore size distribution of 1 : 2 CuO-CB6/Co–Al LDH. The comprehensive data are displayed in Fig. 4f. The 1 : 2 CuO-CB6/Co–Al LDH isotherm demonstrates a typical IV isotherm with an H3-type hysteresis loop, indicating mesoporous properties. 1 : 2 CuO-CB6/Co–Al LDH has a specific surface area of 13.06 $m^2 g^{-1}$, a pore volume of 0.069 $cm^3 g^{-1}$, and a pore size distribution of 13.49 nm. These findings are similar to previous reports on LDH materials.[31]

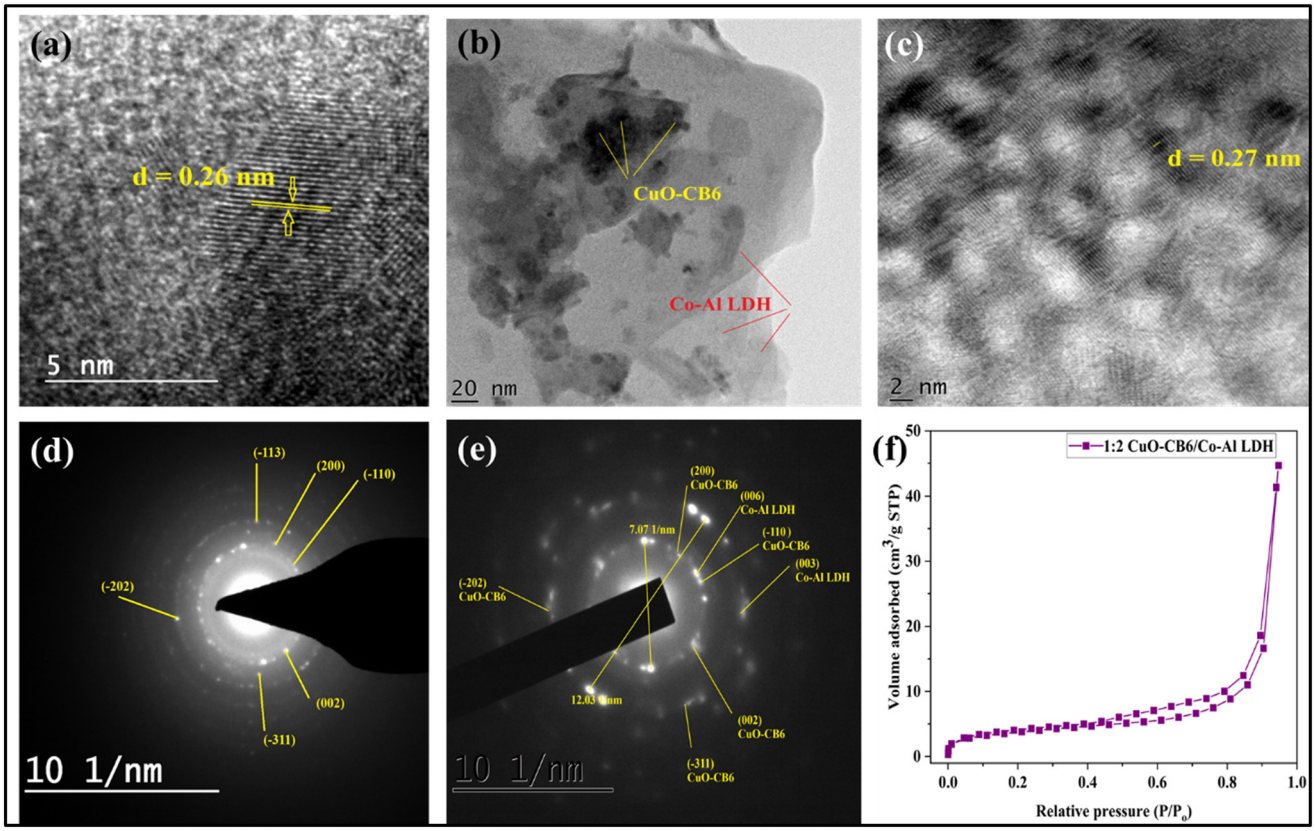

Fig. 4 HR-TEM micrograph of (a) CuO-CB6, (b and c) 1 : 2 CuO-CB6/Co–Al LDH, and SAED patterns of (d) CuO-CB6 & (e) 1 : 2 CuO-CB6/Co–Al LDH. (f) N_2 adsorption/desorption isotherm of 1 : 2 CuO-CB6/Co–Al LDH.

XPS spectroscopic analysis was employed to investigate the chemical bonding and composition of the 1 : 2 CuO-CB6/Co–Al LDH nanocomposite. Fig. 5a reveals the XPS survey scan spectrum of the synthesized 1 : 2 CuO-CB6/Co–Al LDH within the binding energy range of 0–1000 eV. The XPS data of 1 : 2 CuO-CB6/Co–Al LDH across a wide scan range indicated prominent O 1s, Co 2p, Cu 2p, and Cu (Auger) peaks, along with less intense N 1s, C 1s, Cu 3s and 3p peaks. The C 1s XPS spectrum (refer to the ESI† Fig. S4a) was deconvoluted into three peaks at binding energies of 284.63, 287.22, and 288.97 eV, which correspond to C–C, C–O/C═O, and carbonate species in the interlayer, respectively.[27,38,39] The high-resolution O 1s XPS spectrum of 1 : 2 CuO-CB6/Co–Al LDH (refer to ESI† Fig. S4b) is deconvoluted into three peaks corresponding to O–H, O═C, and O–C at 529.25, 530.97, and 532.18 eV, respectively.[27,38,39] The Cu 2p XPS spectrum of 1 : 2 CuO-CB6/Co–Al LDH is displayed in Fig. 5b. Two peaks are observed at 931.87 eV and 951.58 eV, corresponding to Cu $2p_{3/2}$ and Cu $2p_{1/2}$, respectively. 1 : 2 CuO-CB6/Co–Al LDH exhibits shake-up satellite peaks at binding energies of 939.92 eV and 960.98 eV. The Cu $2p_{1/2}$ shake-up satellite peak exhibits a binding energy

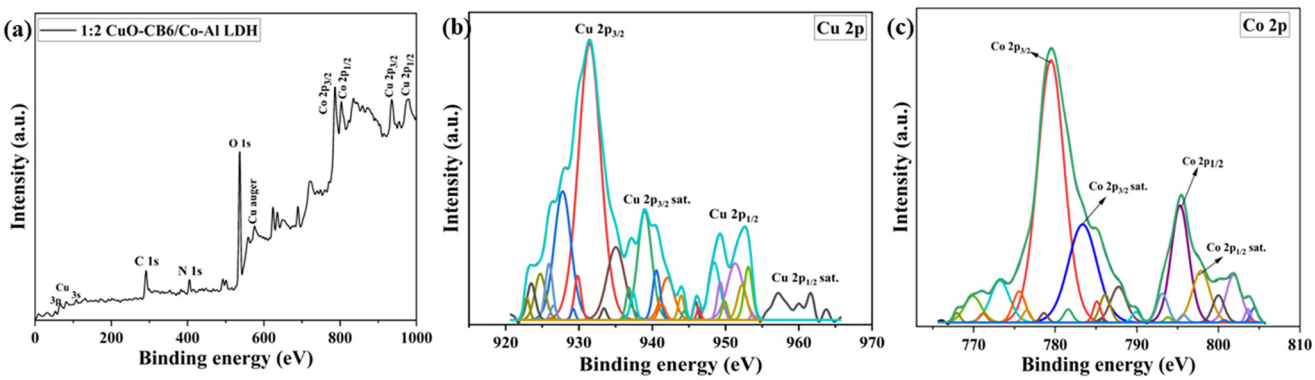

Fig. 5 (a) Wide scan XPS spectra of 1 : 2 CuO-CB6/Co–Al LDH & deconvolution peaks of (b) Cu 2p and (c) Co 2p.

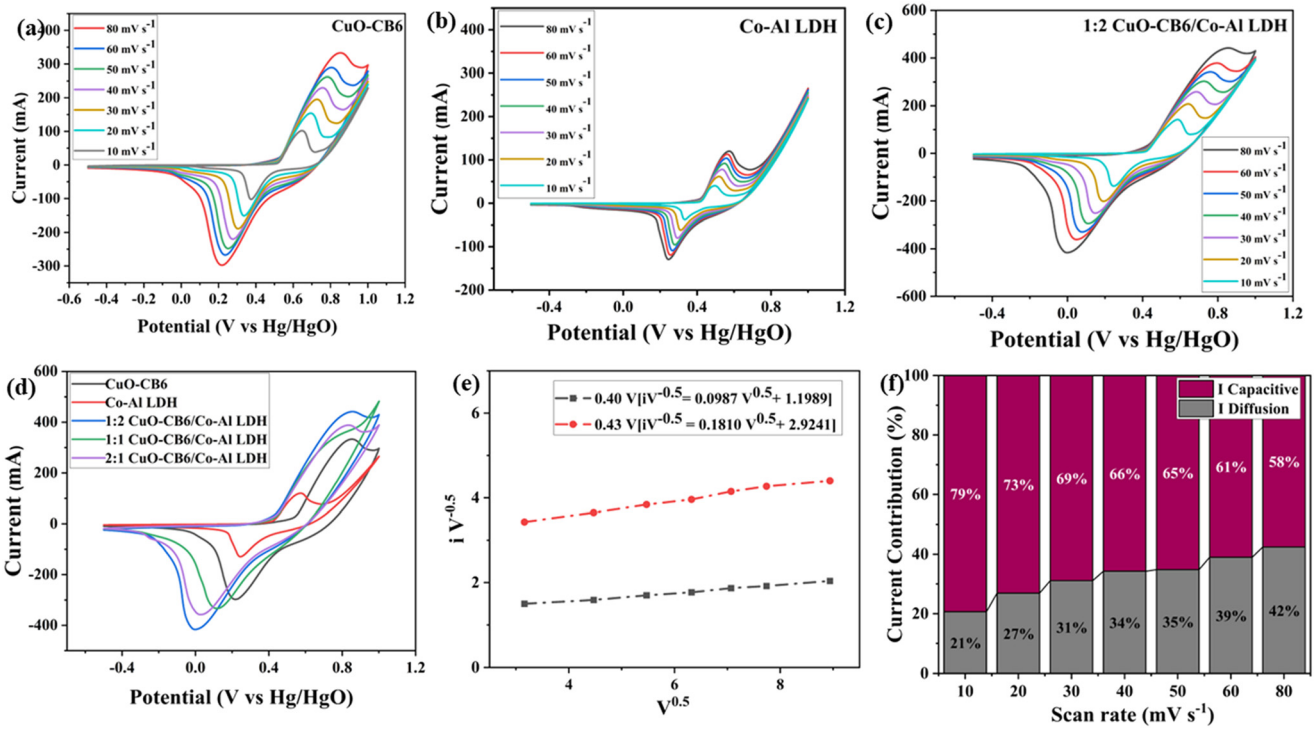

Fig. 6 CV plots of (a) CuO-CB6, (b) Co–Al LDH, and (c) 1 : 2 CuO-CB6/Co–Al LDH in 1 M KOH at current densities of 80, 60, 50, 40, 30, 20, and 10 mV s^{-1}. (d) CV plots of CuO-CB6, Co–Al LDH, and CuO-CB6/Co–Al LDH (1 : 2, 1 : 1, and 2 : 1) at 80 mV s^{-1}. (e) Plot of $V^{0.5}$ *vs.* $iV^{-0.5}$ for 1 : 2 CuO-CB6/Co–Al LDH at 0.40 and 0.43 V. (f) Diffusion controlled and capacitive current for 1 : 2 CuO-CB6/Co–Al LDH with 0.40 V at scan rates of 10, 20, 30, 40, 50, 60, and 80 mV s^{-1}.

approximately 9 eV higher (960.98 eV) than the main peak. Consequently, this indicates that Cu exists in the +2-valence state within 1 : 2 CuO-CB6/Co–Al LDH, consistent with previous studies.[27,40] This confirms the oxidation state and the presence of CuO-CB6 on the layers of Co–Al LDH. Further, Fig. 5c represents the Co 2p XPS peaks of 1 : 2 CuO-CB6/Co–Al LDH. The subsequent two peaks were observed at binding energies of 779.75 eV and 795.88 eV, corresponding to Co $2p_{3/2}$ and Co $2p_{1/2}$, respectively. The satellite peaks of Co $2p_{3/2}$ and Co $2p_{1/2}$ for 1 : 2 CuO-CB6/Co–Al LDH are observed at 783.66 eV and 797.99 eV, respectively. This analysis indicates that the Co ion exists in a divalent Co^{2+} oxidation state.[31,37]

Electrochemical performance of CuO-CB6, Co–Al LDH, and CuO-CB6/Co–Al LDH nanocomposites

The electrochemical behaviors of Co–Al LDH, CuO-CB6, and 1 : 2 CuO-CB6/Co–Al LDH nanocomposite were examined to elucidate the roles of Co–Al LDH and CuO-CB6 in the nanocomposite electrodes. The CV plots for Co–Al LDH, CuO-CB6, and 1 : 2 CuO-CB6/Co–Al LDH can be seen in Fig. 6a–c. Additional details can be found in the ESI† for 1 : 1 CuO-CB6/Co–Al LDH (Fig. S5a†) and 2 : 1 CuO-CB6/Co–Al LDH (Fig. S5b†). The CV profiles of Co–Al LDH, CuO-CB6, and 1 : 2 CuO-CB6/Co–Al LDH demonstrate a pair of distinct redox peaks in 1 M KOH electrolyte solution at varying scan rates (80, 60, 50, 40, 30, 20, and 10 mV s^{-1}) within the voltage range of −0.5 to +1.0 V. The CV plot of bare Co–Al LDH reveals an anodic peak at approximately 0.570 V, signifying the formation of Co(III) oxide (CoOOH), besides a cathodic peak during the reverse scan at 0.246 V, attributed to the reduction of Co(III)/Co(II). The CV plot of bare CuO-CB6 reveals a pair of redox peaks at approximately 0.851 and 0.218 V, confirming the formation of Cu(III) oxide (CuOOH) and Cu(II) oxide (CuO), respectively. The clearly defined redox peaks in the CV curves of active materials underscore the remarkable electrochemical reversibility.[20] The CV plots of CuO-CB6/Co–Al LDH (1 : 2, 1 : 1, and 2 : 1) exhibited an anodic peak at 0.845, 0.784, and 0.826 V, respectively, along with a cathodic peak at 0.016, 0.111, and 0.023 V, respectively as shown in Fig. 6d.

If we look at the CV plot of 1 : 2 CuO-CB6/Co–Al LDH, as the scan rate increases the peak current of the cathode (reduction) and anode (oxidation) rises, indicating that the electron transport at the electrode is uniform and continuous.[38] Fig. 6d shows that the area under the CV curve for 1 : 2 CuO-CB6/Co–Al LDH is significantly larger than pristine Co–Al LDH and CuO-CB6 at the scan rate of 80 mV s^{-1} which is owing to the deposition of CuO-CB6 on Co–Al LDH layers. The combined effects of Co–Al LDH and CuO-CB6 could be the reason for the higher specific capacitance of the 1 : 2 nanocomposite.

A linear correlation was observed for CuO-CB6 and Co–Al LDH (see ESI† Fig. S6a) when we plot the square root of scan rates against anodic/cathodic peak currents. Besides for 1 : 1 CuO-CB6/Co–Al LDH, 2 : 1 CuO-CB6/Co–Al LDH (see ESI† Fig. S6b), and 1 : 2 CuO-CB6/Co–Al LDH (see ESI† Fig. S7), a

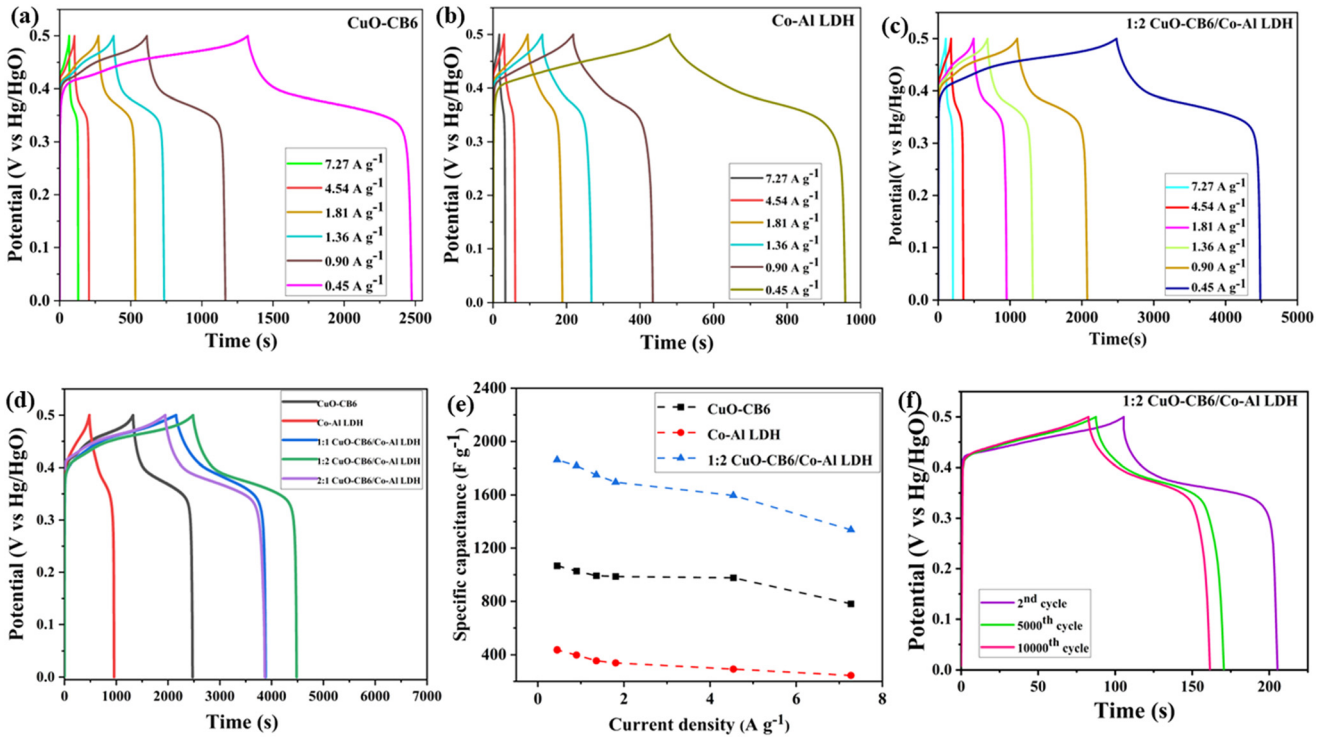

Fig. 7 GCD curves of (a) CuO-CB6, (b) Co–Al LDH, and (c) 1 : 2 CuO-CB6/Co–Al LDH in 1 M KOH at current densities of 7.27, 4.54, 1.81, 1.36, 0.90, and 0.45 A g^{-1}. (d) GCD curves of CuO-CB6, Co–Al LDH, CuO-CB6/Co–Al LDH (1 : 2, 1 : 1, and 2 : 1) at 0.45 A g^{-1}. (e) SC *vs.* current density plots of CuO-CB6, Co–Al LDH, and 1 : 2 CuO-CB6/Co–Al LDH attained from GCD. (f) GCD curve of 1 : 2 CuO-CB6/Co–Al LDH at the 2nd, 5000th, and 10 000th cycle at 7.27 A g^{-1} current density.

significant linearity indicates a rapid electron transfer reaction rate, according to the Randles–Sevcik equation. Regression values for the linear plots that are presented in Fig. S6 and S7† are around 0.99. The anodic and cathodic plots indicate that the processes at the electrodes are diffusion controlled.[41]

Dunn's approach was used to plot $V^{0.5}$ *vs.* $iV^{-0.5}$ for the 1 : 2 CuO-CB6/Co–Al LDH nanocomposite at potentials of 0.40 and 0.43 V, to identify the contributions from diffusion-controlled current and capacitive current (Fig. 6e). Additionally, Fig. 6f represents the percentage contributions from diffusion-controlled current and capacitive current at a potential of 0.40 V for scan rates of 10, 20, 30, 40, 50, 60, and 80 mV s^{-1}. The data clearly shows that as the scan rate increases, the diffusion control process for the 1 : 2 CuO-CB6/Co–Al LDH nanocomposite increases from 21% to 42%.

To obtain a more comprehensive understanding of pseudocapacitance behavior of CuO-CB6/Co–Al LDH nanocomposites, GCD measurements were conducted using 1 M KOH as the electrolyte. Fig. 7a–c illustrate the GCD curves of Co–Al LDH, CuO-CB6, and 1 : 2 CuO-CB6/Co–Al LDH at varying current densities of 7.27, 4.54, 1.81, 1.36, 0.90, and 0.45 A g^{-1}, see ESI† Fig. S8a and b for 1 : 1 CuO-CB6/Co–Al LDH, and 2 : 1 CuO-CB6/Co–Al LDH nanocomposites. The GCD curves of Co–Al LDH, CuO-CB6, and CuO-CB6/Co–Al LDH nanocomposites exhibited a nonlinear characteristic during extended charge durations. The charge–discharge steps indicate a minor internal resistance (IR) drop, accompanied by symmetric charge and discharge curves for composites, demonstrating the pseudocapacitance nature of the nanocomposites. However, the smaller IR drop cannot restrict the composites for high-power applications. Because pseudocapacitive materials have quick charge-transfer kinetics, they frequently have low internal resistance.[42] The specific capacitances for pristine and all the three nanocomposites were analyzed through GCD measurements. The values for Co–AL LDH are 245.14, 278.12, 339.41, 355.43, 398.43, and 435.95 F g^{-1}, and for CuO-CB6, the values are 781.71, 977.13, 986.44, 992.85, 1027.23, and 1067.86 F g^{-1}. The 1 : 2 CuO-CB6/Co–Al LDH configuration shows SC values of 1337.70, 1596.83, 1696.25, 1751.22, 1818.83, and 1862.26 F g^{-1}. The 1 : 1 CuO-CB6/Co–Al LDH configuration shows values of 1235.63, 1322.87, 1378.03, 1398.45, 1448.57, and 1615.12 F g^{-1}. Finally, the 2 : 1 CuO-CB6/Co–Al LDH configuration presents SC values of 1202.20, 1276.43, 1395.06, 1466.96, 1596.40, and 1785.22 F g^{-1} at current densities of 7.27, 4.54, 1.81, 1.36, 0.90, and 0.45 A g^{-1}, respectively. Fig. 7d represents the GCD curves for Co–Al LDH, CuO-CB6, and 1 : 2 CuO-CB6/Co–Al LDH at a current density of 0.45 A g^{-1}. 1 : 2 CuO-CB6/Co–Al LDH exhibited a longer discharge time compared to Co–Al LDH and CuO-CB6, attributed to the improved ion transport of CuO-CB6 confined within the layers of Co–Al LDH. At lower current density, the CuO-CB6/Co–Al LDH nanocomposite-modified electrode exhibits superior electron transport as compared to pristine Co–Al LDH and CuO-CB6.

Fig. 7e represents the plot of charge/discharge current density against SC for Co–Al LDH, CuO-CB6, and 1 : 2 CuO-CB6/Co–Al LDH. The corresponding plots for composites 1 : 1 CuO-CB6/Co–Al LDH, and 2 : 1 CuO-CB6/Co–Al LDH are shown in ESI† Fig. S9. The SC values decrease as the current density increases because electrolyte ions take a longer time to diffuse into the inner active regions of the electrode material at high current densities.[38] The SC value of pure Co–Al LDH and CuO-CB6 is significantly lower than that of the nanocomposite, suggesting that the deposition of CuO-CB6 onto the surface layers of Co–Al LDH plays a crucial role in influencing the SC. This observation suggests that the rate capacity of the 1 : 2 CuO-CB6/Co–Al LDH nanocomposite is outstanding. The 1 : 2 CuO-CB6/Co–Al LDH composite-modified electrode exhibit enhanced SC due to the higher capacitance of the nanocomposite that is attributed to its improved charge transport behavior with a greater number of active sites.

The long-term cycling stability of 1 : 2 CuO-CB6/Co–Al LDH was validated through sustained charge–discharge cycles at a constant current density of 7.27 A g^{-1}. Fig. 7f illustrates the GCD plot of 1 : 2 CuO-CB6/Co–Al LDH for the 2nd, 5000th, and 10 000th cycles at a current density of 7.27 A g^{-1}. The GCD plot clearly shows that there is a drop in SC value from 1474.50 to 1241.70 F g^{-1} as the number of cycles increases from the 2nd to 5000 cycles. Further, the drop continues slowly and reaches the SC value of 1171.35 F g^{-1} at the 10 000th cycle. Initially, the abundance of new electroactive sites might facilitate rapid electrochemical redox reactions, resulting in prolonged charge–discharge cycles that enhance cycling stability.[43] However, persistent charging and discharging may result in the degradation of the electrode material, thereby causing a reduction in SC.[38] Therefore, the degradation of the electrode material may be the reason for the drop in SC value from the 2nd to 5000 cycles. However, there is only a slight drop from the 5000th to 10 000th cycles. 1 : 2 CuO-CB6/Co–Al LDH exhibited enhanced coulombic efficiency, retaining 79% of the initial SC after 10 000 cycles. Consequently, the remarkably stable 1 : 2 CuO-CB6/Co–Al LDH nanocomposite is suitable for application as an electrode material in long-term storage devices.

The electrochemical mechanism of CuO-CB6 and the Co–Al LDH nanocomposite is mainly owing to the synergistic interaction between the individual properties of each constituent material. The distinct morphology and particle size of CB6-capped CuO NPs along with the electrostatic interactions between Co–Al LDH and CuO-CB6 substantially improve the overall electrical conductivity of the nanocomposite. The enhanced conductivity promotes quick electron transport which is essential for effective electrochemical processes. The layered structure of Co–Al LDH provides a high surface area and abundant interlayer spacing. This interlayer spacing can efficiently accommodate ions and CB6-capped CuO NPs, thereby enhancing the total capacity for electrochemical reactions.[44] The electrochemical reactions within the composite likely encompass a combination of processes. CuO executes reversible redox processes, like $Cu^{2+} + 2e^- \rightleftharpoons Cu$, which contribute to its charge storage capacity. The layered structure of Co–Al LDH facilitates the reversible intercalation and deintercalation of ions within its interlayer spaces, thereby improving charge storage capacity. This synergistic property of CuO-CB6 and the Co–Al LDH nanocomposite leads to a notable enhancement in electrochemical capacity relative to the individual components, positioning it as a promising candidate for diverse energy storage applications.

The resistance of ion diffusion in CuO-CB6/Co–Al LDH electrode materials was evaluated using EIS analysis. Ionic diffusion resistance governs the rate of ion migration inside the electrode material. Ionic diffusion resistance refers to the passage of ions through the pores of an electrode. Therefore, lower ionic diffusion resistance enhances ion transport leading to superior electrochemical performance.[45] Moreover, electronic resistance that arises from the inherent resistance of the electrode material is equally important.[46] A lower electrical resistance increases rapid electron transport, which speeds up charge–discharge processes. EIS measurements are carried out in the frequency range of 0.1 Hz to 100 kHz with an AC perturbation of 10 mV to understand the electronic and ionic resistance of these materials. The faradaic reaction at the electrode/electrolyte interface induces the charge transfer resistance (R_{ct}), which forms a semicircle in the high-to-middle frequency region of the impedance spectrum. Conversely, a low-frequency straight line is indicative of Warburg impedance.[47] The diameter of the half-circle shows the R_{ct} at the interface between the electrode and electrolyte. This value is caused by faradaic reactions and double layer capacitance on the sample surfaces. A larger diameter in the high-frequency region signifies high resistance, whereas the slope of the line reflects capacitive behavior. Fig. 8a displays the Nyquist plots of Co–Al LDH, CuO-CB6, and 1 : 2 CuO-CB6/Co–Al LDH in 1 M KOH electrolytic solution along with the equivalent circuit diagram, see ESI† Fig. S10 for 1 : 1 CuO-CB6/Co–Al LDH and 2 : 1 CuO-CB6/Co–Al LDH nanocomposites. The circuit diagram of EIS $R(CR)(QR)(CR)$ is a widely utilized model for the analysis of EIS data. R denotes the solution resistance (R_s), which encompasses the resistance of the electrolyte positioned between the working and reference electrode. CR denotes the double-layer capacitance (C_{dl}) at the interface between the electrode and electrolytes. QR denotes a parallel configuration of a resistor (R) and a constant phase element (Q). The constant phase element (CPE) simulates capacitive behavior that is not ideal. This component of the circuit usually signifies the charge transfer resistance (R_{ct}) associated with the electrochemical reaction taking place at the electrode surface. CR is a parallel combination of a resistor and a capacitor that can represent a variety of phenomena depending on the system. This encompasses the resistance and capacitance related to a secondary reaction or diffusion process occurring within the electrode material. This configuration is frequently employed in EIS to represent complex impedance characteristics.

The solution resistance (R_s) values for Co–Al LDH, CuO-CB6, 1 : 2 CuO-CB6/Co–Al LDH, 1 : 1 CuO-CB6/Co–Al LDH, and 2 : 1

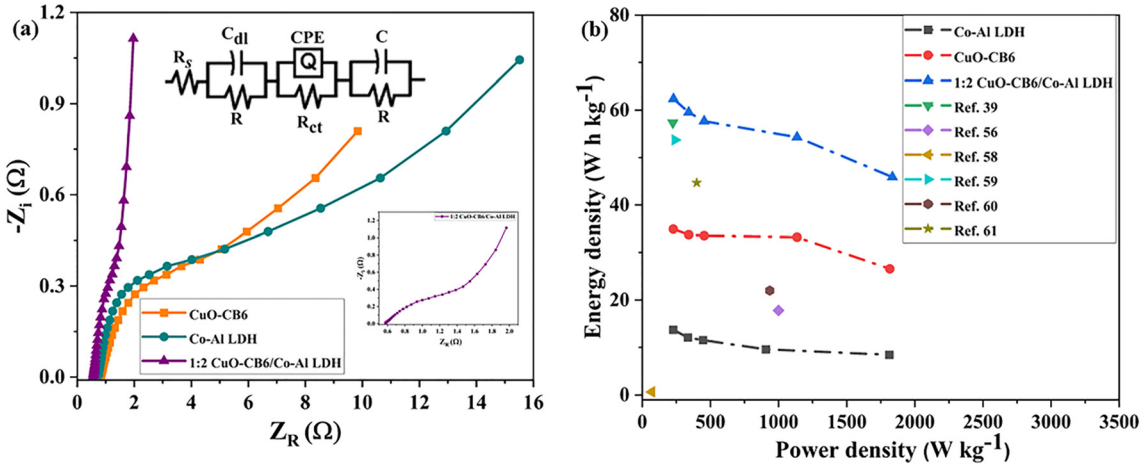

Fig. 8 (a) Nyquist plots of CuO-CB6, Co–Al LDH, and 1 : 2 CuO-CB6/Co–Al LDH with the equivalent circuit diagram. (b) Ragone plot of CuO-CB6, Co–Al LDH, and 1 : 2 CuO-CB6/Co–Al LDH compared with other similar materials in the literature.

CuO-CB6/Co–Al LDH, as determined by the Nyquist plots from the intersection of curves with the actual impedance axis, are 0.78, 0.83, 0.58, 0.70, and 0.67 Ω, respectively. 1 : 2 CuO-CB6/Co–Al LDH reveals a lower R_s value than pristine CuO-CB6 and Co–Al LDH. The inset in Fig. 8a demonstrates that 1 : 2 CuO-CB6/Co–Al LDH exhibits superior electrical conductivity, as indicated by its lower resistance value compared to the other samples. The Nyquist plots presented in Fig. 8a exhibit capacitive behavior, as indicated by the straight line observed in the low-frequency region.[39] The elevated slope for 1 : 2 CuO-CB6/Co–Al LDH further substantiates its superior capacitive performance compared to the other electrodes.

The Ragone plot illustrates the relationship between energy density (ED) and power density (PD) for CuO-CB6, Co–Al LDH, and 1 : 2 CuO-CB6/Co–Al LDH nanocomposite as shown in Fig. 8b, see ESI† Fig. S11 for 1 : 1 CuO-CB6/Co–Al LDH and 2 : 1 CuO-CB6/Co–Al LDH nanocomposites. In addition, the Ragone plot in Fig. 8b was compared with other similar materials in the literature.[38,48–52] The relationship was determined by the discharge curve at current densities of 0.45, 0.90, 1.36, 1.81, 4.54, and 7.27 A g^{-1}. CuO-CB6 recorded a maximum ED of 36.30 W h kg^{-1} with a corresponding PD of 113.52 W kg^{-1} at a current density of 0.45 A g^{-1}. In the same current density, Co–Al LDH exhibits an ED of 15.04 W h kg^{-1} at a PD of 113.26 W kg^{-1}. 1 : 2 CuO-CB6/CoAl-LDH nanocomposite also showed a high ED of 63.87 W h kg^{-1} and a PD of 114.19 W kg^{-1} at a current density of 0.45 A g^{-1}, as shown in Fig. 8b. These values are compared with previously reported copper oxide and LDH-based electrode materials. This comparison conveys the performance of 1 : 2 CuO-CB6/Co–Al LDH nanocomposite in a clear and concise manner, indicating better understanding of its potential applications and useful insights for future research.

Table 1 presents the comparative electrochemical performance of the 1 : 2 CuO-CB6/Co–Al LDH nanocomposite against other copper oxide-based and LDH-based electrode materials. Table 1 indicates that 1 : 2 CuO-CB6/Co–Al LDH exhibited superior specific capacity and maintained 79% cycle stability at a current density of 7.27 A g^{-1}. These results confirm the suitability of 1 : 2 CuO-CB6/Co–Al LDH nanocomposite as an excellent electrode material for high-performance supercapacitors.

Conclusions

This study involves the incorporation of CB6-stabilized CuO NPs onto Co–Al LDH *via* a solvothermal method to produce three different CuO-CB6/Co–Al LDH 1 : 1, 1 : 2, and 2 : 1 nanocomposites. The synthesis of CuO-CB6/Co–Al LDH nanocomposites was validated through advanced characterization techniques, including XRD, FT-IR, HR-TEM,

Table 1 A comparative analysis of copper oxide-based and LDH-based electrode materials for specific capacitance investigation

Electrode material	Electrolyte	Specific capacitance	Current density	Cyclic performance	Reference
Cu/CuO@C	1 M KOH	432.5 F g^{-1}	1 A g^{-1}	88.6% after 8000 cycles	48
CC@NiCuOx	2 M KOH	2937 mF cm^{-2}	5 mA cm^{-2}	82.5% after 5000 cycles	53
CF@CuOx@NiCuOx	1 M KOH	623.5 mF cm^{-2}	2 mA cm^{-2}	80.16% after 1500 cycles	49
g-C_3N_4@CoAl-LDH	2 M KOH	343.3 F g^{-1}	5 A g^{-1}	93% after 6000 cycles	54
CoAl LDH-PANI	1 M KOH	528 F g^{-1}	10 A g^{-1}	42.7% after 6000 cycle	55
Co–Al LDH/TiO_2	2 M KOH	611.4 F g^{-1}	10 mA cm^{-2}	81% after 2000 cycles	56
CAN-LDH-NS/rGO	2 M KOH	1296 F g^{-1}	1 A g^{-1}	90.5% after 1000 cycles	57
GO@CoAl LDH	6 M KOH	1725.71 F g^{-1}	1 A g^{-1}	95% after 5000 cycles	58
NCA-LDH@NCS@CC	6 M KOH	1775 F g^{-1}	1 A g^{-1}	79.6% after 10 000 cycles	59
CoAl-LDH/FGN	6 M KOH	1222 F g^{-1}	1 A g^{-1}	88% after 3000 cycles	60
1 : 2 CuO-CB6/Co–Al LDH	1 M KOH	1862 F g^{-1}	0.45 A g^{-1}	79% after 10 000 cycles	Current work

FE-SEM-EDX, and XPS analysis. The electrochemical performance of the synthesized CuO-CB6/Co–Al LDH nanocomposites was assessed through CV, GCD, and EIS measurements. The 1 : 2 CuO-CB6/Co–Al LDH nanocomposite exhibited a specific capacitance of 1862 F g^{-1} at a current density of 0.45 A g^{-1}, as determined by GCD analysis. GCD and EIS analyses reveal improved electrical conductivity and cycle stability for the 1 : 2 CuO-CB6/Co–Al LDH nanocomposite as compared to the pristine materials as well as 1 : 1 and 2 : 1 nanocomposites. The incorporation of CuO-CB6 onto Co–Al LDH resulted in improved electrical conductivity and reduced charge transfer resistance in the 1 : 2 CuO-CB6/Co–Al LDH nanocomposite. Additionally, GCD data indicated that the 1 : 2 CuO-CB6/Co–Al LDH nanocomposite exhibited a long-term cycling stability of 79% even after 10 000 cycles at a current density of 7.27 A g^{-1}. The synthesized 1 : 2 CuO-CB6/Co–Al LDH nanocomposite can serve as a promising electrode material for supercapacitor applications.

Data availability

The data supporting this article have been included as part of the ESI.†

Author contributions

Anakha D. R.: data curation, formal analysis, investigation, writing original draft. Ashika K. M. and Vyshnavi T. V.: supporting for synthesis and data curation. M. Ananthkumar: resources and supporting data curation. R. Yamuna: conceptualization, resources, supervision, review & editing. The final manuscript was revised and approved by all authors.

Conflicts of interest

There are no conflicts to declare.

Acknowledgements

We are extremely grateful to the CoE-AMGT centre (MHRD, New Delhi) for providing instrumental facilities.

Notes and references

1 K. K. Patel, T. Singhal, V. Pandey, T. P. Sumangala and M. S. Sreekanth, *J. Energy Storage*, 2021, **44**, 103366.
2 Poonam, K. Sharma, A. Arora and S. K. Tripathi, *J. Energy Storage*, 2019, **21**, 801–825.
3 V. Prabu, K. Geetha, R. Sekar and M. Ulaganathan, *Energy Technol.*, 2023, **11**, 2201345.
4 B. Gangaja, S. Nair and D. Santhanagopalan, *ACS Sustainable Chem. Eng.*, 2021, **9**, 4711–4721.
5 A. G. Olabi, Q. Abbas, A. Al Makky and M. A. Abdelkareem, *Energy*, 2022, **248**, 123617.
6 J. Libich, J. Máca, J. Vondrák, O. Čech and M. Sedlaříková, *J. Energy Storage*, 2018, **17**, 224–227.
7 W. Raza, F. Ali, N. Raza, Y. Luo, K. H. Kim, J. Yang, S. Kumar, A. Mehmood and E. E. Kwon, *Nano Energy*, 2018, **52**, 441–473.
8 S. Karthikeyan, B. Narenthiran, A. Sivanantham, L. D. Bhatlu and T. Maridurai, *Mater. Today: Proc.*, 2021, **46**, 3984–3988.
9 H. W. Park and K. C. Roh, *J. Power Sources*, 2023, **557**, 232558.
10 G. Yao, N. Zhang, Y. Zhang and T. Zhou, *J. Nanopart. Res.*, 2021, **23**, 57.
11 A. Afif, S. M. Rahman, A. Tasfiah Azad, J. Zaini, M. A. Islam and A. K. Azad, *J. Energy Storage*, 2019, **25**, 100852.
12 D. Gao, Z. Luo, C. Liu and S. A. Fan, *Green Energy Environ.*, 2023, **8**, 972–988.
13 A. Muzaffar, M. B. Ahamed, K. Deshmukh and J. Thirumalai, *Renewable Sustainable Energy Rev.*, 2019, **101**, 123–145.
14 Q. Wang and D. Ohare, *Chem. Rev.*, 2012, **112**, 4124–4155.
15 Y. Zhang and S. Wei, *J. Nanopart. Res.*, 2019, **21**, 14.
16 Q. Ding, J. Li, S. Li, J. Wang, W. Huang, S. Sun, Y. Xu and H. Li, *J. Energy Storage*, 2023, **67**, 107556.
17 Y. Ma, X. Xie, W. Yang, Z. Yu, X. Sun, Y. Zhang, X. Yang, H. Kimura, C. Hou, Z. Guo and W. Du, *Adv. Compos. Hybrid Mater.*, 2021, **4**, 906–924.
18 P. Gaikwad, N. Tiwari, R. Kamat, S. M. Mane and S. B. Kulkarni, *Mater. Sci. Eng., B*, 2024, **307**, 117544.
19 Y. Wang, D. Yang, J. Lian, T. Wei and Y. Sun, *J. Alloys Compd.*, 2018, **741**, 527–531.
20 L. Kunhikrishnan and R. Shanmugam, *J. Mater. Sci.: Mater. Electron.*, 2020, **31**, 21528–21539.
21 Y. Zhan, J. Bai, F. Guo, H. Zhou, R. Shu, Y. Yu and Q. Lin, *J. Alloys Compd.*, 2021, **885**, 161014.
22 R. Eivazzadeh-Keihan, R. Taheri-Ledari, M. S. Mehrabad, S. Dalvand, H. Sohrabi, A. Maleki, S. M. Mousavi-Khoshdel and A. E. Shalan, *Energy Fuels*, 2021, **35**, 10869–10877.
23 M. W. Ahmad, S. Anand, A. Fatima, D. J. Yang and A. Choudhury, *Polym. Adv. Technol.*, 2021, **32**, 4070–4081.
24 W. Peng, H. Li and S. Song, *ACS Appl. Mater. Interfaces*, 2017, **9**, 5204–5212.
25 Z. P. Diao, Y. X. Zhang, X. D. Hao and Z. Q. Wen, *Ceram. Int.*, 2014, **40**, 2115–2120.
26 J. Kim, I. S. Jung, S. Y. Kim, E. Lee, J. K. Kang, S. Sakamoto and K. Kim, *J. Am. Chem. Soc.*, 2000, **122**, 540–541.
27 A. D. Rajeeve, V. T. Veetil, P. K. K. Namboori, R. Yamuna and A. Rajendran, *J. Mol. Liq.*, 2024, **415**, 126323.
28 P. Guoxiang, X. Xinhui, L. Jingshan, C. Feng, Y. Zhihong and F. Hongjin, *Appl. Clay Sci.*, 2014, **102**, 28–32.
29 M. U. Trivedi, C. K. Patlolla, N. M. Misra and M. K. Pandey, *Catal. Lett.*, 2019, **149**, 2355–2367.
30 V. V. T. Padil and M. Černík, *Int. J. Nanomed.*, 2013, 889–898.
31 Z. Liu, L. Teng, L. Ma, Y. Liu, X. Zhang, J. Xue, M. Ikram, M. Ullah, L. Li and K. Shi, *RSC Adv.*, 2019, **9**, 21911–21921.
32 D. Renuga, J. Jeyasundari, A. S. Athithan and Y. B. A. Jacob, *Mater. Res. Express*, 2020, **7**, 045007.
33 B. Teklu, S. K. Kadiri and S. Vidavalur, *Results Chem.*, 2023, **6**, 101152.
34 Y. Tokudome, A. Obata, N. Kitagawa, K. Nagatsuka, E. Gorai, Y. Maehashi and T. Kasuga, *Mater. Adv.*, 2024, **5**, 2926–2933.

35 P. Guoxiang, X. Xinhui, L. Jingshan, C. Feng, Y. Zhihong and F. Hongjin, *Appl. Clay Sci.*, 2014, **102**, 28–32.
36 J. H. Cha, E. B. Park, S. W. Han, Y. D. Kim and D. Y. Jung, *Chem. – Asian J.*, 2019, **14**, 446–453.
37 X. Guo, Z. Fan, Y. Wang and Z. Jin, *Surf. Interfaces*, 2021, **24**, 101105.
38 A. D. Rajeeve, R. Yamuna, M. Vinoba and M. Bhagiyalakshmi, *Langmuir*, 2023, **39**, 17688–17699.
39 X. Li, Z. Lin, C. Wang, H. Wang, S. Feng, T. Li and Y. Ma, *Chem. Eng. J.*, 2024, **484**, 149430.
40 S. M. Pawar, B. S. Pawar, A. I. Inamdar, J. Kim, Y. Jo, S. Cho and H. Im, *Mater. Lett.*, 2017, **187**, 60–63.
41 Y. Li, S. Chang, X. Liu, J. Huang, J. Yin, G. Wang and D. Cao, *Electrochim. Acta*, 2012, **85**, 393.
42 M. Diantoro, I. Istiqomah, Y. A. Fath, N. Mufti, N. Nasikhudin, W. Meevasana and Y. B. Alias, *Micromachines*, 2022, **13**, 1989.
43 X. Sun, J. Wang, C. Huang, Y. Wu, J. Hou, Y. Situ and H. Huang, *Electrochim. Acta*, 2022, **428**, 140929.
44 D. Tichit and M. G. Álvarez, *Chem. Eng.*, 2022, **6**, 45.
45 N. P. Ngidi, A. F. Koekemoer and S. S. Ndlela, *J. Energy Storage*, 2024, **89**, 111638.
46 Y. Sun, J. Sun, J. S. Sanchez, Z. Xia, L. Xiao, R. Chen and V. Palermo, *Chem. Commun.*, 2023, **59**, 2571–2583.
47 B. A. Mei, J. Lau, T. Lin, H. Tolbert, B. S. Dunn, L. Pilon and L., *J. Phys. Chem. C*, 2018, **122**, 24499–24511.
48 R. Mathaiyan, A. A. Nechikott, S. B. M. K., P. K. Nayak and S. Kancharla, *J. Mater. Chem. A*, 2024, **12**, 28107–28118.
49 Y. Ren, T. Zhu, Y. Liu, Q. Liu and Q. Yan, *Small*, 2021, **17**, 2008047.
50 X. Bai, F. Sun, L. Ma, J. Shen, Z. Jiang, D. Xu and H. Zhang, *Ionics*, 2024, 1–10.
51 C. Jing, X. D. Liu, K. Li, X. Liu, B. Dong, F. Dong and Y. Zhang, *J. Energy Chem.*, 2021, **52**, 218–227.
52 H. Xuan, G. Zhang, T. Liang, R. Wang, J. Yang, J. Yang and Y. Wu, *J. Alloys Compd.*, 2021, **873**, 159801.
53 T. Zhu, J. Pan, Z. An, R. Zhe, Q. Ou and H. E. Wang, *J. Mater. Chem. A*, 2022, **10**, 20375–20385.
54 S. Sanati and Z. Rezvani, *Chem. Eng. J.*, 2019, **362**, 743–757.
55 G. Yang, T. Takei, S. Yanagida and N. Kumada, *Molecules*, 2019, **24**, 976.
56 H. Zhu and J. Zhang, *Inorg. Chem. Commun.*, 2022, **145**, 110027.
57 Z. Huang, S. Wang, J. Wang, Y. Yu, J. Wen and R. Li, *Electrochim. Acta*, 2015, **152**, 117–125.
58 C. Jing, Y. Huang, L. Xia, Y. Chen, X. Wang, X. Liu, B. Dong, F. Dong, S. Li and Y. Zhang, *Appl. Surf. Sci.*, 2019, **496**, 143700.
59 Y. Li, X. Yan, W. Zhang, W. Zhou, Y. Zhu, M. Zhang, W. Zhu and X. Cheng, *J. Electroanal. Chem.*, 2022, **905**, 115982.
60 W. Peng, H. Li and S. Song, *ACS Appl. Mater. Interfaces*, 2017, **9**, 5204–5212.